In-situ neutron diffraction study of wrought and selective laser melted maraging stainless steels

Michella Alnajjar, Frédéric Christien, Cédric Bosch, Krzysztof Wolski, A. Dominic Fortes, Mark Telling

In-situ neutron diffraction study of wrought and selective laser melted maraging stainless steels.

Michella Alnajjar[a], Frédéric Christien[a,*], Cédric Bosch[a], Krzysztof Wolski[a], A. Dominic Fortes[b], Mark Telling[b,c]

[a] Mines Saint-Etienne, Univ Lyon, CNRS, UMR 5307 LGF, Centre SMS, F - 42023 Saint-Etienne, France

[b] ISIS Facility, Rutherford Appleton Laboratory, Chilton, OX11 0QX, UK

[c] Department of Materials, University of Oxford, Parks Road, Oxford, UK

*: corresponding author, frederic.christien@emse.fr

Abstract

Bulk phase transformations and dislocation density were monitored in a maraging stainless steel on a bulk level using in-situ neutron diffraction up to 1340°C, i.e. 30°C below the melting temperature. Three materials with different initial microstructure and/or different composition were studied: wrought, as-built SLM-ed (selective laser melted) and re-austenitized SLM-ed. In contrast to the wrought martensitic steel, the as-built SLM-ed steel was essentially ferritic. However, re-austenitized SLM-ed steel recovered the usual martensitic microstructure. A δ-ferritic domain above 1200°C was confirmed for all the materials studied. However, the amount of δ-ferrite at the melting point strongly depends upon steel composition. Additionally, it was shown that the initial microstructure of the steel (ferritic or martensitic) has little to no influence on re-austenization. Dislocation densities were estimated from diffraction peak broadening. The ferritic as-built SLM material contains a high dislocation density (~$4x10^{14}$ m^{-2}), which is however far less than in the martensitic materials (~$5x10^{15}$ m^{-2}). Dislocations start to annihilate from 550°C / 600°C in all the materials studied, but a measurable dislocation density of ~10^{13} m^{-2} is still observed at 950°C / 1000°C.

Keywords: Neutron diffraction, Bulk phase transformation, Selective laser melting, Laser beam melting, Additive manufacturing, 17-4PH, Maraging stainless steels, Dislocation density

Introduction

Wrought 17-4PH steel is a martensitic precipitation hardenable stainless steel. It is widely used in a variety of applications such as aerospace, medical and food industries, due to its high strength and relatively good corrosion resistance. A fully martensitic microstructure is obtained after a solution heat treatment in the austenitic domain (~1050 °C) followed by quenching to room temperature. In order to improve the mechanical properties of this steel, a subsequent tempering treatment in the range of 480-620°C is usually applied, which will allow hardening by copper precipitates [1–3]. Recently, this steel has been produced via additive manufacturing (AM), more specifically selective laser melting (SLM). The microstructure of 17-4PH steel obtained using this technology has been the subject of several studies [4–10] reporting that SLM-ed microstructures are usually different from their wrought counterparts. In particular, it was shown in several studies that the SLM-ed 17-4PH steel fabricated under argon could be mainly ferritic in the as-built state [7–11]. This was explained in [8] by the by-passing of the austenite phase, the δ-ferritic solidification microstructure not transforming to austenite during cooling, because of the very high cooling rate of the SLM process (10^5 - 10^6 K/s). The by-passing of austenite precludes the formation of martensite, which results in an essentially δ-ferritic microstructure at room temperature. It should be mentioned however that the effects of process parameters, building atmosphere and alloy composition on the intensity of this by-passing effect are not currently completely understood.

It is well known that solidification of stainless steels can follow different paths depending on whether austenite or δ-ferrite is the primary solid phase to form [12]. This solidification path is strongly dependent on alloy composition. In addition, it has been shown that for stainless steels solidifying into δ-ferrite, some amounts of δ-ferrite can be retained at room temperature, especially in welding

conditions where the cooling rate is usually high (> 100 ~ 1000 K/s) [12]. The austenite by-passing effect observed for SLM-ed 17-4PH would be an extreme case of δ-ferrite retention due to extremely high cooling rates of SLM (~10^6 K/s). However this interpretation assumes that the 17-4PH steel solidifies into δ-ferrite, but to our knowledge, no experimental data about the phase constitution of that alloy at very high temperature (i.e. between 1200°C and the melting temperature) is available to support that assumption, the current data being limited to 1050°C [13,14]. In addition, the standard composition of that steel allows some variations in alloy element content within some percents. These variations can significantly affect the phase constitution close to the melting temperature and hence the solidification path. We propose in this work to study the phase constitution of the 17-4PH steel close to the melting temperature for two different compositions, both of them complying with the standard composition of the 17-4PH steel.

In-situ diffraction studies of steels between 1200°C and the melting temperature are very rare in literature, apart from a few studies related to welding [15–19]. In addition, those studies usually do not provide any quantitative data of phase constitution, apart from the study by Mayr et al. [16]. One of the difficulties of those studies is that, in metals, elemental evaporation is pronounced above 1200°C, which can significantly affect the specimen composition over a certain depth. If conventional X-rays are used, the depth of analysis (typically of the order of 1 µm) is usually lower than the depth affected by evaporation. In that case the diffracted signal comes from a material which is different in composition from the bulk material of interest, making the analysis irrelevant [20]. To avoid that issue, highly penetrating radiation, like neutrons, is needed. The depth of penetration of neutrons in steels is as high as some centimeters, which makes neutron diffraction particularly suitable for very high temperature experiments on metals.

For industrial applications, the 17-4PH SLM-ed steel is usually heat treated after SLM processing. This post-building heat treatment can include re-austenitizing at 1050°C + ageing in the range 480°C-620°C. Alternatively, only the ageing treatment is sometimes done. In the latter case, i.e. without

post-building re-austenitizing, careful examination of the as-built microstructure is needed to check whether the martensitic, or possibly the ferritic, microstructure is present. In case a ferritic microstructure is obtained in the as-built state, re-austenizing is mandatory to recover the martensitic microstructure. However it was observed by Rowolt et al. [21] that the austenitizing process was retarded for a 17-4PH SLM-ed steel, compared to a conventional one. This suggested that the initial microstructure (martensitic or ferritic) could affect the re-austenitizing conditions, which we also propose to confirm, or otherwise, in this study.

Martensitic steels usually show high dislocation density, mainly arising from the martensitic transformation itself [22–25]. For the 17-4PH steel, dislocation densities as high as $4x10^{15}$ m^{-2} were reported [25] in the as-quenched state. Whether the same level of dislocation density can be obtained in the as-built state after SLM processing is questionable, especially if the microstructure obtained is ferritic. Due to the very high cooling and heating rates experienced during SLM edification, high stresses can develop in the part being built, which can actually result in high dislocation densities in the as-built state. So far the measurements of dislocation densities in SLM iron-based alloys are limited to austenitic stainless steels (304 and 316), as shown in the review paper by Zuback and Debroy [26]. The values obtained are in the range of 10^{14} to 10^{15} m^{-2} [27–30], i.e. close to those of martensitic materials.

In summary, the objectives of this paper are the following:

(1) to quantitatively study the phase constitution of two 17-4PH steel compositions close to the melting temperature (presence and amount of equilibrium δ-ferrite and/or austenite), and to show how it is related to steel composition. This will clarify the possible solidification paths of the steel.

(2) to study how the initial room temperature microstructure (martensite or ferrite) possibly affects the re-austenization treatment,

(3) to determine the dislocation densities in the different materials studied and to study how dislocations annihilate upon heating.

Materials and methods

The materials used in this study were wrought and SLM-ed 17-4PH stainless steels. The wrought material is a commercial 17-4PH steel from UGINE (cast # 818025). Samples for neutron diffraction were cut from a 15 mm diameter rod. They were studied after a solution heat treatment at 1050°C for 1 h followed by a water quench. Concerning the SLM-ed 17-4PH steel, samples were cut from cylinders having 16 mm diameter and 105 mm length (Figure 1) fabricated in an SLM machine of type EOS M270. The fabrication was done in an argon purging environment. The longitudinal axis of the cylinder was horizontal, i.e. perpendicular to the building direction Z, as shown in Figure 1. The SLM-ed steel was studied in the as-built condition and after a re-austenization heat treatment at 1050 °C for 1 h followed by a water quench. The chemical composition of all three materials is given in Table 1. The full composition of the wrought material is indicated (data from the steel provider) in the first line of Table 1. Additional measurements were conducted on both wrought and SLM-ed materials (lines 2 and 3 of Table 1). These measurements were carried out using X-ray fluorescence (XRF) (FISCHERSCOPE X-Ray XAN-FD) for elements Ni, Cr and Cu, combustion elemental analysis (CEA) for C, S (LECO CS 444/LS), N and O (LECO TC-436), and inductively coupled plasma optical emission spectroscopy (ICP-OES) for Mn, Si and Nb. Table 1 also indicates the standard composition of 17-4PH steel (AISI 630).

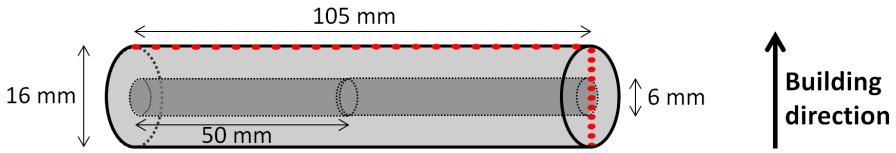

Figure 1: Shape of SLM specimen in light grey. The dark grey cylinders indicate how the neutron diffraction specimens were cut. The red dots indicate the areas of EDX analysis conducted to check the chemical homogeneity of the SLM specimen at the macroscale.

Table 1: Chemical composition (wt. %) of wrought and SLM-ed 17-4PH stainless steels

17-4PH		C	Ni	Si	P	Mn	Cr	Cu	S	N	O	Nb	Fe
Wrought	Provider Data sheet	0.031	4.82	0.31	0.016	0.81	15.61	3.12	0.02	-	-	0.21	Bal.
	XRF/CEA	0.026	4.95	-	-	-	16.18	3.09	0.021	0.033	0.007	-	Bal.
SLM-ed (as-built and re-austenitized)	XRF/CEA/ ICPOES	0.030	4.16	0.71	0.008	0.32	16.11	3.73	0.003	0.033	0.046	0.30	Bal.
Standard specification (AISI 630)		<0.07	3.0 5.0	<1.0	<0.04	<1.0	15 17.5	3.0 5.0	<0.03	-	-	0.15 0.45	Bal.

For microstructural observations, Electron BackScatter Diffraction (EBSD) observations were conducted at 20 kV on specimens polished down to 1200 grit and then electropolished using 94% ethanol + 6% perchloric acid as electrolyte at 25 V for 60 s. EBSD data were processed using the MTEX software package [31] working under Matlab so as to extract the phase and orientation maps. From the EBSD data obtained on martensite, the parent austenite microstructure was reconstructed using the algorithm developed by Nyyssönen et al. [32], which can be used in the MTEX/Matlab environment. This algorithm determines whether some neighboring grains, based on their orientation, share the same prior austenitic grain orientation or not. The Kurdjumov-Sachs relationships [33] are used as a first estimation of the martensite/austenite orientation relationship (OR). However the actual OR is iteratively determined by the algorithm and can slightly differ from Kurdjumov-Sachs. The nature of different boundaries present in the martensitic microstructure (block boundaries, packet boundaries and former austenitic grain boundaries [34]) can then be extracted from the reconstruction procedure. In this work, those different types of boundaries were overlaid to the orientation maps of the martensitic materials.

Energy Dispersive X-ray Spectroscopy (EDX) was conducted at 20 kV for local chemical analysis of the as-built SLM-ed material. For macroscale analysis, a series of 20x20 µm areas were analysed in the scanning mode as indicated in Figure 1 (eleven areas along the cylinder diameter and 23 areas along the cylinder length). To ensure a good counting statistics, the counting time per area was of three

minutes. For microscale analysis, EDX mapping was conducted on a 80x105 µm area at a resolution of 1536x2048 pixels. The counting time for the microscale mapping was of 10 hours for the whole map. EDX profiles were also acquired on a diffraction specimen after heating to 1340°C to determine the depth of material affected by evaporation (Figure 2).

Neutron diffraction data was collected using the High Resolution Powder Diffractometer (HRPD) at the ISIS facility, Rutherford Appleton Laboratory (RAL), UK [35]. Each neutron diffraction measurement was performed while continuously heating the specimen in-situ (i.e. in the neutron instrument) under high vacuum ($4x10^{-6}$ mBar) to avoid any surface oxidation. The samples used for the experiment were cylinders of 6 mm diameter and of 50 mm length. For accurate temperature control, a type C thermocouple was inserted into a hole drilled directly into the sample. Typical temperature gradients expected along the sample's 50 mm vertical axis during measurement had been ascertained prior to the neutron experiment using offline test apparatus. Above 1300 °C, the temperature was found to be homogeneous within 15 to 20 °C along said axis. The specimens were therefore only heated to 1340°C since previous dilatometry experiments have shown that 17-4PH steel starts to melt at about 1370°C [8]. Unless otherwise stated, the heating rate chosen was 5 K/min (a compromise between achieving near-equilibrium conditions and keeping the experiment duration reasonable) and the acquisition time was 1 min per pattern, unless otherwise stated.

The depth of material affected by elemental evaporation was measured using EDX profiling on the cross-section of a diffraction specimen after heating to 1340°C. Figure 2 shows that preferential evaporation strongly affects the materials composition over a depth of about 20 µm. The surface vicinity is strongly depleted in chromium and copper, and enriched in iron, nickel and silicon. However the affected depth is limited to 20 µm, which can be considered negligible as neutrons penetrate the whole specimen diameter (6 mm).

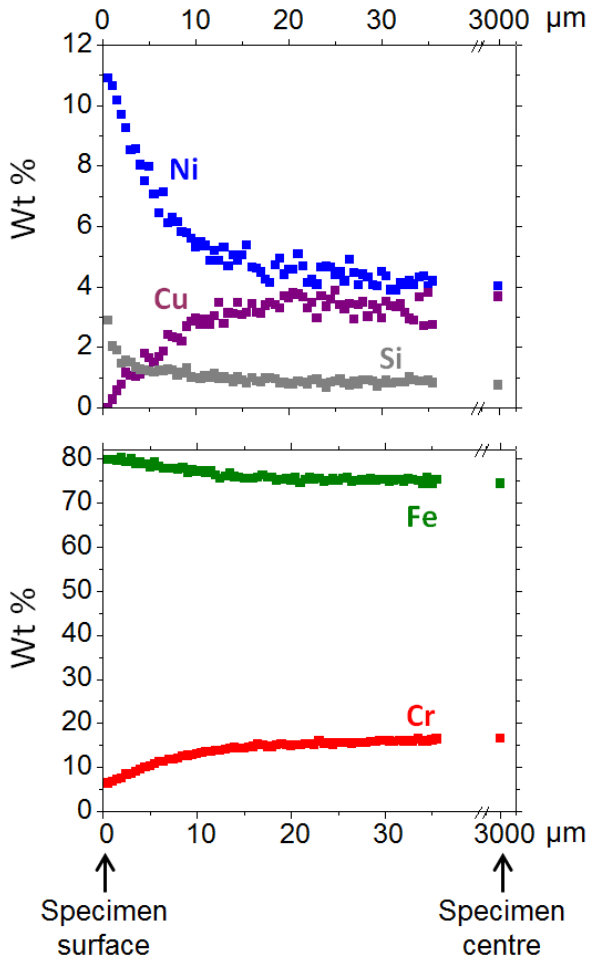

Figure 2: Composition profiles obtained using EDX at 20 kV on the cross-section of a diffraction specimen after heating to 1340°C.

The 'raw' neutron time-of-flight data were 'focused' to a common scattering angle (2θ = 168.33° for the highest resolution backscattering data used here) and then both normalized to the incident spectrum and corrected for detector efficiency using a V:Nb standard. This initial data processing was carried out using the Mantid suite of diffraction algorithms [36,37]. In backscattering, the time-of-flight range employed (30-130 ms) provides us with a diffraction pattern, effectively scattered intensity vs. interplanar d-spacing between ~ 0.65 to 2.65 Å, allowing the detection of the main diffraction peaks of the body centered cubic (BCC) and face centered cubic (FCC) phases.

As discussed in [6,11,13], and in contrast to other steels, the tetragonality of martensite or ferrite in 17-4PH steel is usually not detectable because of the low carbon content. Consequently, martensite

and ferrite were considered BCC here, not tetragonal. A complete multiphase Rietveld refinement of selected neutron diffraction patterns was conducted using GSAS/Expgui [38,39] to extract the BCC and FCC phase mass fraction. Spherical-harmonic models to eighth order (yielding three extra refinable terms due to the cubic symmetry) were used in order to take account of possible preferential crystal orientations. For all the patterns processed, the texture index J as defined in [38] was in the range from 1.00 to 1.03, except one of them being 1.09. This indicates a very slight texture in any case ($J = 1$ for a perfectly randomized powder and $J = \infty$ for a single crystal [38]).

Considering the large number of diffraction patterns acquired in this study, this refinement procedure was not practical for all of them. Instead, only the most important datasets were selected for refinement (about 10 patterns for each experiment, covering the whole range of possible phase constitution). It was shown that the phase fractions obtained from the complete Rietveld refinement can be approximated by the simple following equation:

$$\boldsymbol{BCC\%} = \frac{\boldsymbol{A_{BCC(110)}}}{\boldsymbol{A_{BCC(110)} + 1.40\, A_{FCC(111)}}} \times \boldsymbol{100} \qquad (1)$$

where $A_{BCC(110)}$ and $A_{FCC(111)}$ are the peak intensities (peak areas) of the BCC (110) and the FCC (111) lines respectively. Here the 1.40 term was adjusted so as to obtain the best agreement between the BCC mass fractions obtained from Rietveld refinement and those obtained using Eq. 1 (Figure 3). It was found that for 26 patterns out of 29, the difference is within 6%, which is reasonable. For all the patterns that were not processed using Rietveld refinement, the BCC mass fraction was determined using Eq. 1.

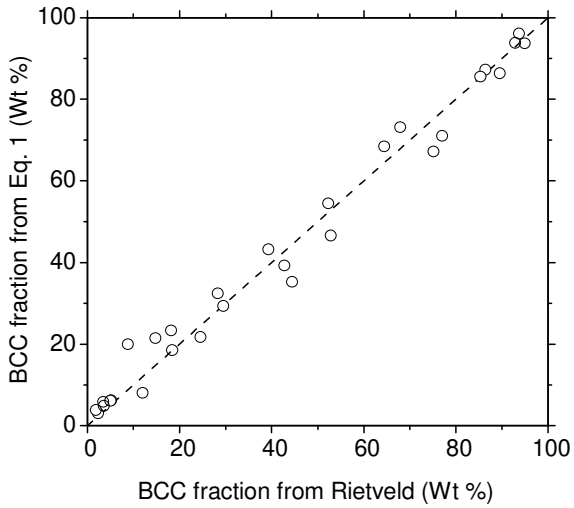

Figure 3: Correlation between the BCC mass fractions obtained from Rietveld refinement and those obtained from Eq. 1.

The dislocation density ρ in the BCC phase can be correlated to the average peak broadening β using the following Stibitz equation (Eq. 2) [40,41]:

$$\boldsymbol{\rho = \frac{3E}{\mu b^2(1+2\upsilon^2)}\left(\frac{\beta}{d}\right)^2} \quad (2)$$

$$\boldsymbol{\beta = \beta_t - \beta_i}$$

where E is the Young's modulus, μ is the shear modulus with $E/\mu \approx 2.5$ for the materials studied here, d is the interplanar spacing of a particular diffraction line, β_t is the total peak Full Width at Half Maximum (FWHM), β_i is the instrumental peak FWHM, obtained at high temperature (> 1300°C) when peak refining is complete. The burger vector b is equal to 0.249 nm and the Poisson's coefficient υ is 0.25. The determination of β/d was done on four peaks corresponding to the BCC crystallographic planes (220), (211), (200) and (110) and then their average was computed. More details are given about the methodology in a previous study by Christien et al. [25].

Results and discussion

Figure 4 shows the macroscale composition profiles obtained using EDX along diameter and length of a SLM-ed specimen. Very homogeneous composition is shown at the macroscale. No significant variation in alloy composition is observed, neither along the building direction, nor perpendicularly to it. The slight random variations observed for the low concentration elements (Mn and Si) are within the statistical uncertainty of the EDX measurement (±0.05%). It should also be noted that the average composition measured from EDX is in very good agreement with the bulk composition shown in Table 1. Figure 5 presents a series of microscale elemental maps measured using EDX. The composition at the microscale is observed to be very homogeneous. No evidence of solidification segregation is found at that scale. This is in good agreement with some previous reports on SLM-ed 17-4PH steel [8,9]. The absence of segregation suggests that solidification occurred here in the regime of "absolute stability" described in [42]. This regime is observed for very high cooling rates, which is the case here, and is characterized by diffusionless solidification and solutal trapping, resulting in a segregation-free microstructure.

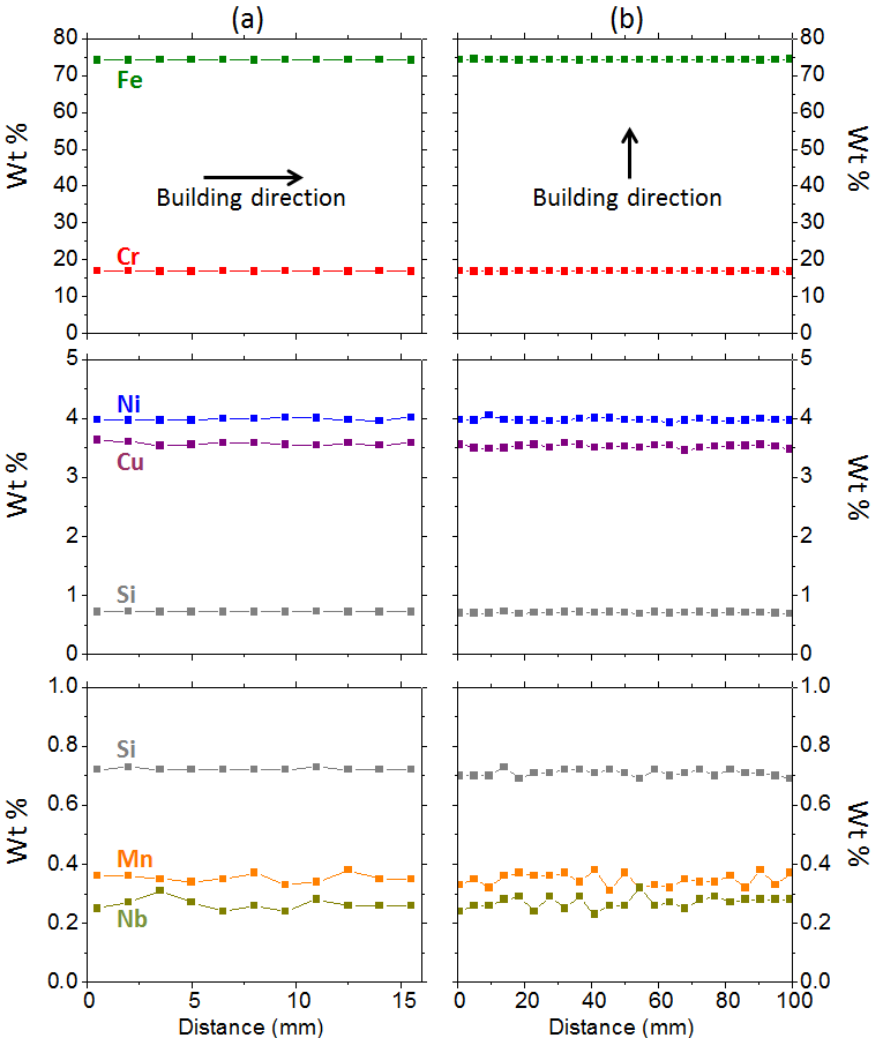

Figure 4: Macroscale composition profiles obtained using EDX at 20 kV on an as-built SLM-ed specimen. (a): along the specimen diameter (i.e. building direction). (b): along the specimen length (see red dots in Figure 1 to locate the areas of analysis). Each point on a profile corresponds to a 20x20 µm area analyzed.

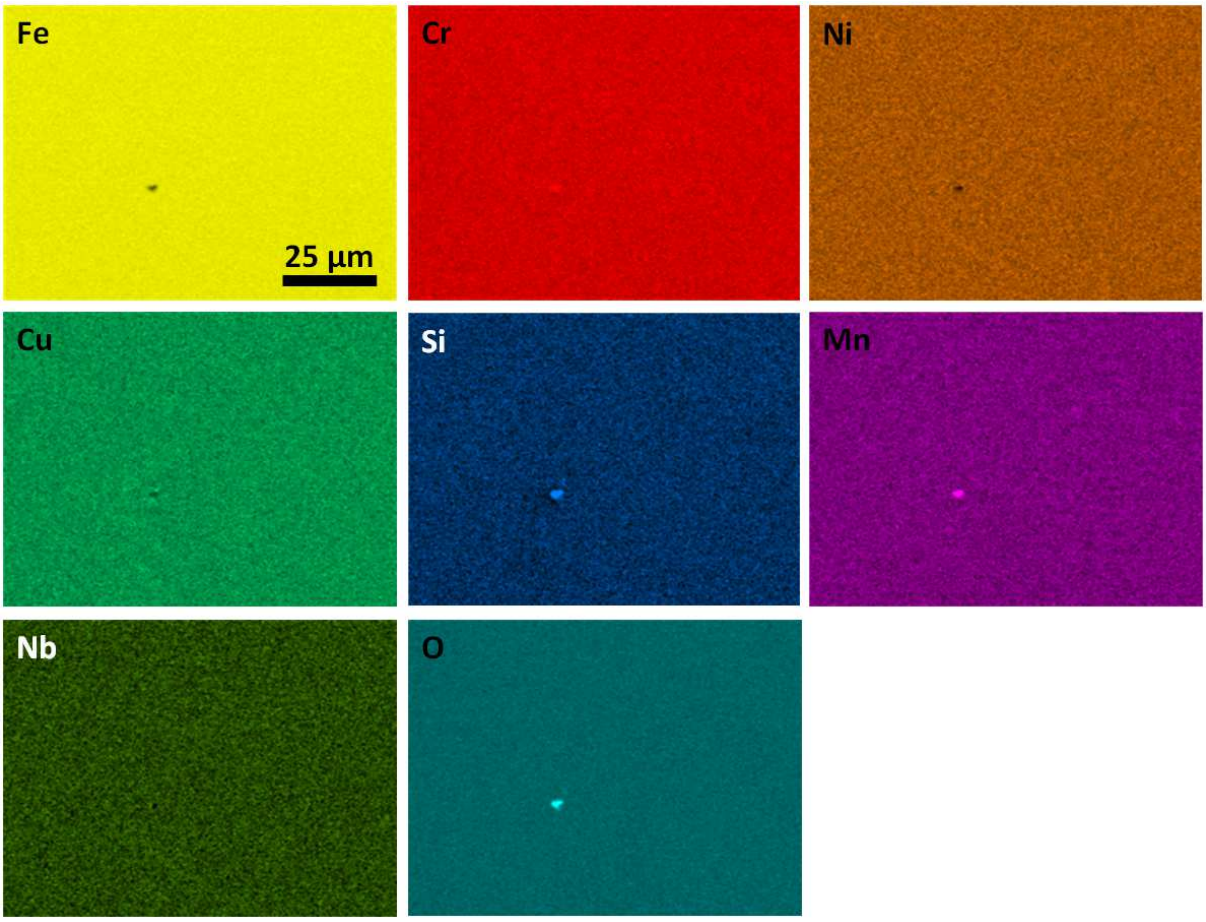

Figure 5: Microscale elemental maps obtained using EDX on the as-built SLM-ed material. The Kα x-ray line was used for all elements, except for Nb (Lα). The Si- and Mn-rich particle is an oxide.

Figure 6 shows the EBSD orientation maps and phase maps, obtained from the three materials studied. The main phase present in the three materials is BCC. The amount of FCC phase (austenite) was 0.03% and 5.1% in the wrought and as-built SLM-ed materials respectively. No austenite was detected in the re-austenitized SLM-ed material. However the fractions of austenite mentioned here should be considered with caution. The retained austenite in quenched martensitic materials is usually present as nanometric lathy islands [43,44] that cannot be quantitatively resolved using EBSD. This makes it very difficult to quantify the fraction of retained austenite in martensitic steels using EBSD. For the as-built SLM-ed material (which is not martensitic but mainly ferritic as explained later), the amount of austenite obtained from EBSD is 5.1%. However Figure 6(e) shows that austenite is present as a finely dispersed phase and the density of non-indexed pixels is significantly higher in the austenite-rich areas. This suggests that the fraction of austenite obtained from EBSD may be underestimated for that material as well.

As expected, the wrought material was found martensitic, as shown by the BCC orientation map in Figure 6(a): the laths of martensite are gathered into different blocks and packets [45] inside the same prior austenitic grain. The block and packet boundaries (thin lines), as well as the former austenitic boundaries (thick lines) were identified from the austenite reconstruction algorithm [32]. In contrast to the wrought steel, the microstructure of as-built SLM-ed 17-4PH steel (Figure 6(b)) does not show a typical martensitic microstructure with packets and blocks. Instead, the microstructure consists mainly of coarse grains, some of them elongated along the building direction. The reconstruction algorithm, when used for this microstructure, fails in finding any possible common parent austenitic orientation for any group of neighboring BCC grains. This shows, from a crystallography point of view, that the microstructure of the as-built SLM-ed material is not martensitic. It can then be deduced that the as-built SLM-ed 17-4PH steel has a ferritic microstructure. This is in agreement with the observations conducted on SLM-ed 17-4PH steel fabricated under argon in several previous studies [7–10,46], which showed extensive retention of δ-ferrite. Figure 6(c) shows the microstructure of the SLM-ed material after re-austenization (at 1050°C

for 1 hour followed by a water quench). The usual arrangement in blocks and packets inside former austenite grains is observed, which means that the martensitic microstructure has been recovered. Again here, the block and packet boundaries (thin lines), as well as the former austenitic boundaries (thick lines), were identified from the austenite reconstruction algorithm [32]. This implies that the initial δ-ferrite transformed to austenite during heating and subsequent holding for 1 h at 1050°C, and that the austenite then transformed to martensite during cooling, resulting in the observed microstructure.

Figure 7 shows examples of diffraction patterns acquired on the three materials at different temperatures. At room temperature, the diffraction patterns are similar for the three materials, confirming that the main phase is BCC in any case, although austenite peaks are clearly visible in the SLM-ed as-built material and, to a lesser extent, in the wrought one. In addition, it can be noticed that the BCC peaks are much broader in the two martensitic materials (wrought and re-austenitized SLM-ed) than in the ferritic one (SLM-ed as built). This will be commented later. At 970°C, the wrought material is entirely austenitic, while a significant (110) BCC peak is still visible in the two other materials. At 1100°C, the three materials are fully austenitic. At 1340°C, an increase of the BCC peaks is observed in all the materials, which demonstrates the existence of δ-ferrite. However the austenite peaks at 1340°C are higher in the wrought material.

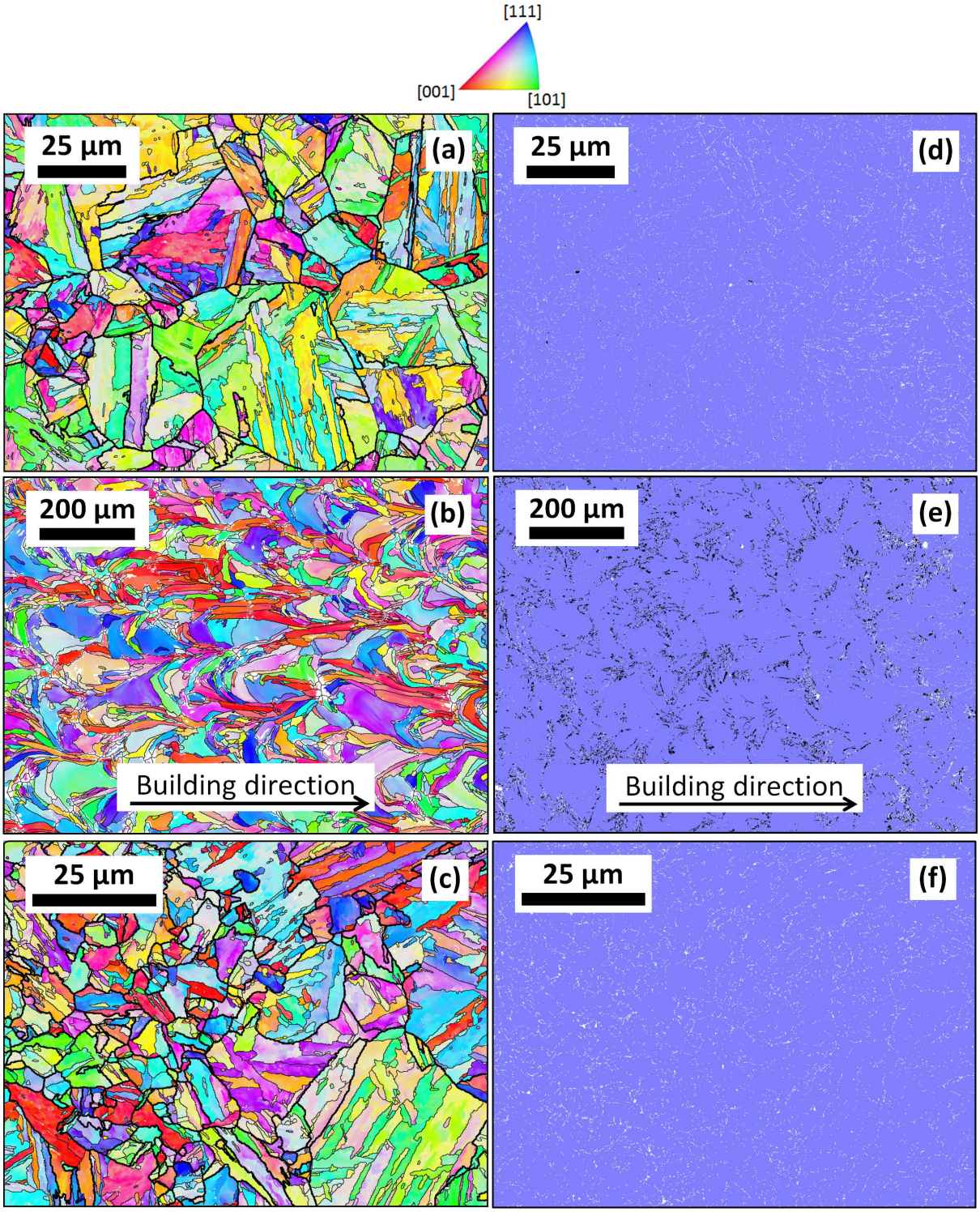

Figure 6: EBSD orientation maps of the BCC phase in (a) wrought 17-4PH steel showing a typical martensitic microstructure, (b) as-built SLM-ed 17-4PH steel showing coarse grain ferritic microstructure and (c) re-austenitized SLM-ed 17-4PH steel showing martensitic microstructure. Attention is drawn to the much larger scale in (b). In (a) and (c), the thin lines represent the block and packet boundaries of martensite and the thick lines represents the former austenitic grain boundaries, identified from the austenite reconstruction algorithm [32]. The orientation maps are Z Inverse Pole Figures, Z being the steel rod axis in the case of the wrought steel and the building direction in the case of the SLM-ed steel. (d), (e) and (f) are the corresponding phase maps of the wrought, as-built SLM-ed and re-austenitized SLM-ed steels respectively. The BCC and FCC phases are in blue and black respectively. Non-indexed areas are in white.

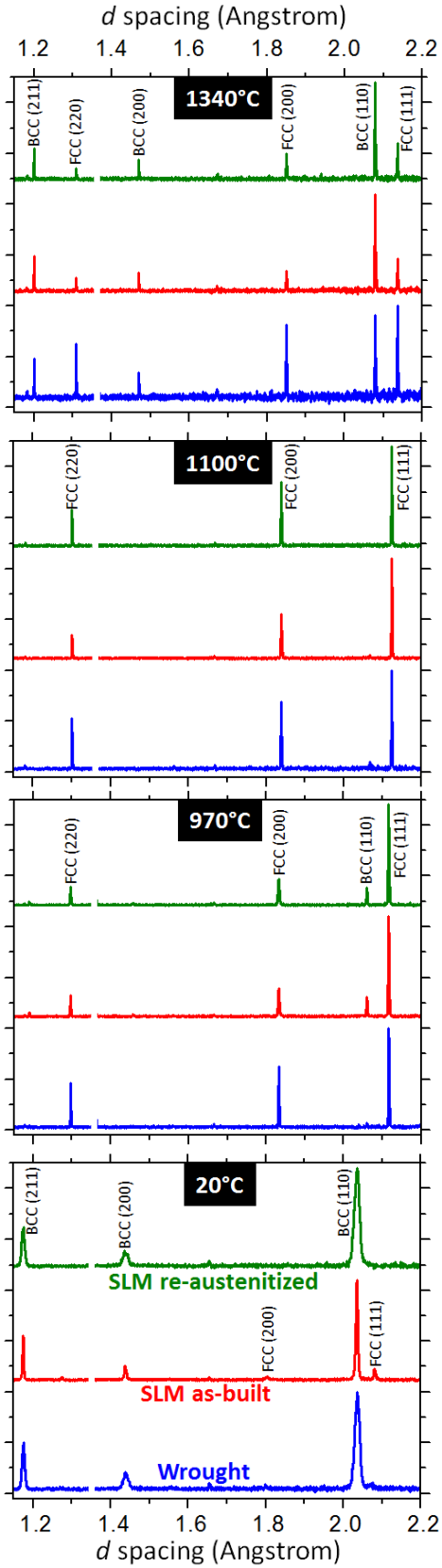

Figure 7: Examples of normalized diffraction patterns obtained on the three 17-4PH steels studied (wrought, as-built SLM and re-austenitized SLM) at 20°C, 970°C, 1100°C and 1340°C.

Figure 8 shows the temperature dependence of the BCC mass fraction during heating to 1340 °C for wrought steel and re-austenitized SLM-ed steel. According to the microstructural characterization done at room temperature using EBSD (Figure 6), both wrought and re-austenitized SLM-ed steels have an initial martensitic microstructure. On the other hand, their chemical composition is slightly different (Table 1). The initial amount of retained austenite is about 3% in the wrought steel. Austenite was not detected in the re-austenitized SLM-ed steel. During heating, the martensite-to-austenite transformation starts at approximately Ac_1~620 °C for both steels. This Ac_1 is similar to the one previously reported by Christien *et al.* [13] using neutron diffraction measurements on the same steel. Then, the phase transformation in both steels progresses in two stages characterized by two different kinetic behaviors, i.e. slopes. This two stage martensite-to-austenite transformation has already been reported by Bojack et al. [47] who studied the austenization in a supermartensitic stainless steel using dilatometry. According to those authors, the two-stage phase transformation may be due to the partitioning of elements in the BCC and FCC phases. The stability range of austenite for the wrought steel is between 970 °C and 1300°C, while, for the re-austenitized SLM-ed steel, it is roughly between 1050 °C and 1200 °C. Based on these observations, it is deduced that the austenite is more stable in the wrought steel. As heating continues, the phase transformation from austenite to δ-ferrite starts at 1300 °C for the wrought steel and at 1200 °C for the re-austenitized SLM-ed steel. For the wrought steel, the fraction of δ-ferrite is 20 % at 1340 °C and about 40 % after extrapolation to the melting temperature (1370°C [8]), while, for the re-austenitized SLM-ed steel, the fraction of δ-ferrite is significantly higher: 75 % at 1340 °C and about 90 % after extrapolation to the melting temperature. This result proves that 17-4PH steel can be essentially δ-ferritic at the melting point. However Figure 8 also shows that above 1300°C the amount of delta δ-ferrite is significantly different in the two steels although both the compositions are in the standard specifications (Table 1). This may be related to slight differences in composition of the two steels. To check that assumption, the chromium and nickel equivalents, that gather the effect of all FCC-

stabilizing (Ni, Mn, C, N) and BCC-stabilizing elements (Cr, Si, Nb) respectively, were determined from the following equations [12]:

$$Cr_{Eq} = Cr + 6Si + 5Nb \quad (3)$$

$$Ni_{Eq} = Ni + 0.31Mn + 22C + 14.2N + Cu \quad (4)$$

where the element symbols represent the weight percentage. For the wrought material, when two values of concentration are available for a given element, the average of the two values was considered. The chromium and nickel equivalents obtained are shown in Table 2. No significant difference in the nickel equivalent is found. In contrast, the chromium equivalent differs by 3.1%. The main contribution to that difference is from the silicon content, which is higher by a factor of 2.5 in the SLM-ed material. To estimate how this difference can affect the phase constitution at high temperature (close to the melting temperature), the isothermal section of the ternary Fe-Cr-Ni diagram at 1300°C was considered [48,49]. The two points in Figure 9 represent the composition of the wrought and SLM-ed materials of this study, considering their nickel and chromium equivalent content. It is found that the two alloys lie in the δ–γ biphasic domain, each of them being close to opposite domain boundaries. The main phase expected in the wrought material is austenite, whereas that in the SLM-ed material is δ-ferrite, which is in good agreement with our experimental observations. In that range of composition and temperature, the ternary diagram shows that the δ-γ domain is very narrow. This means that a small difference in composition, here a difference of a few percents in the chromium content, can completely change the phase composition of the alloy.

Table 2: Chromium and nickel equivalents in Wt % in the wrought and SLM-ed 17-4PH steels

	Cr_{Eq}	Ni_{Eq}
Wrought	18.8	9.3
SLM-ed	21.9	9.1

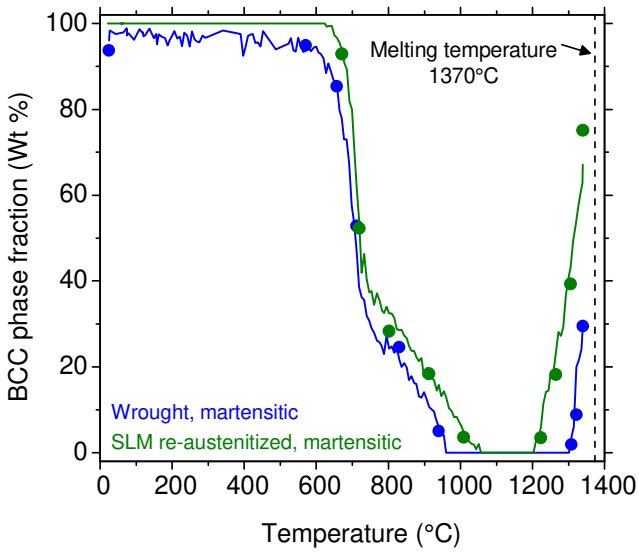

Figure 8: BCC phase fraction in 17-4PH steel (wrought and re-austenitized SLM) obtained using neutron diffraction as a function of temperature during heating to 1340°C at 5K/min. The two materials have the same initial microstructure (martensite), but different chemical composition. The lines indicate phase fractions obtained from Eq.1 whereas the points indicate phase fractions obtained from Rietveld refinement.

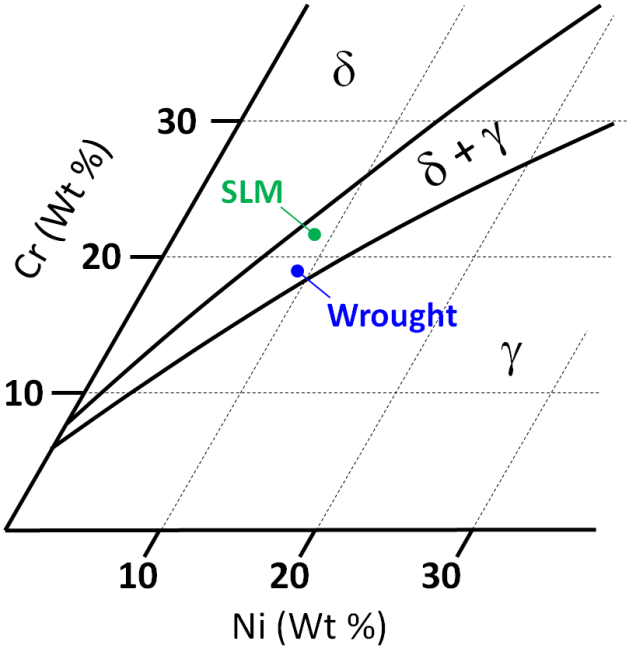

Figure 9: Location of the wrought and SLM 17-4PH steels in the isothermal section of the Fe-Cr-Ni diagram at 1300°C [48,49] using their Cr and Ni equivalent contents.

Figure 10 shows the temperature dependence of the BCC mass fraction during heating to 1340°C for as-built and re-austenitized SLM-ed steels. The two steels have exactly the same composition here. On the other hand, based on the microstructural characterization done at room temperature using EBSD (Figure 6), as-built SLM-ed steel has an initial δ-ferritic microstructure, while the re-austenitized SLM-ed steel has an initial martensitic microstructure. As expected, Figure 10 shows that both SLM-ed steels have mainly a BCC (ferrite or martensite) structure at the beginning of heating. However, the initial austenite content is about 10% in the as-built SLM-ed steel, whereas austenite is not detected in the re-austenitized SLM-ed steel. During heating, the BCC to FCC phase transformation took place similarly for both steels regardless of their initial microstructure (ferrite or martensite). Since both steels have identical chemical composition, their austenite stability range was almost similar. At higher temperatures, the onset of the austenite-to-δ ferrite transformation was identical for both SLM-ed steels (~1200°C). They even reached the same level of δ ferrite content at 1340°C (75%). By extrapolating the curve, it is found that both SLM-ed steels have a 90% ferritic microstructure at the melting temperature.

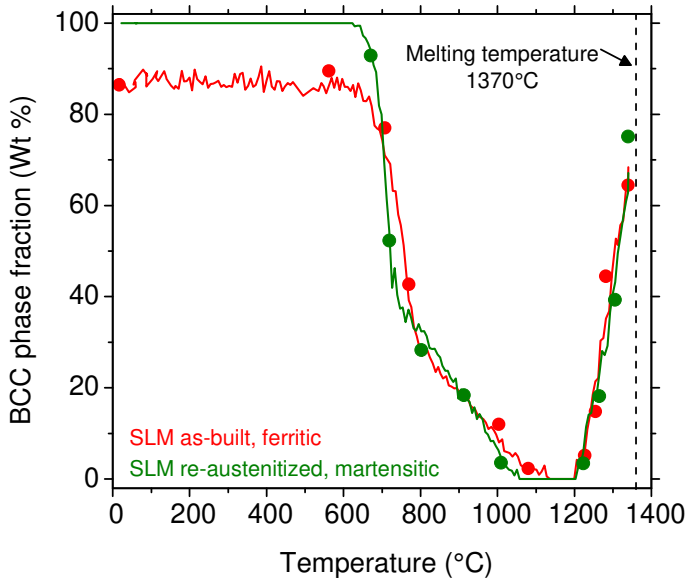

Figure 10: BCC phase fraction in 17-4PH steel (as-built SLM and re-austenitized SLM) obtained using neutron diffraction as a function of temperature during heating to 1340°C at 5K/min. The two materials have the same composition but different initial microstructure (ferrite and martensite). The lines indicate phase fractions obtained from Eq.1 whereas the points indicate phase fractions obtained from Rietveld refinement.

The effect of the initial microstructure (ferritic or martensitic) on austenization was also studied in Figure 11 in fast heating conditions. In this experiment, specimens of as-built SLM-ed steel and re-austenitized SLM-ed steel were heated to and maintained at 1050°C for 30 minutes. The heating rate chosen here was faster than previously used (i.e. 50 K/min instead of 5 K/min) so as to exacerbate possible differences in the kinetics of austenization between the two initial microstructures. Figure 11 shows that annealing at 1050°C allows complete austenization for both materials. In addition, the kinetics of austenization is very similar in the two cases, although completion is obtained slightly later for the as-built SLM-ed material. This result is in contrast to the observations reported by Rowolt et al. [21], who showed that re-austenitizing was retarded for a SLM-ed 17-4PH steel, compared to a conventional one.

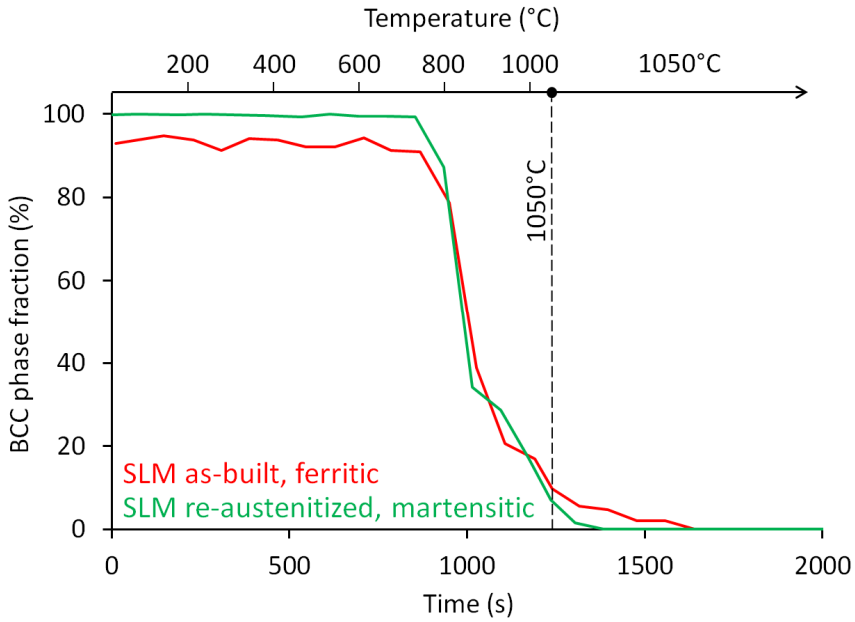

Figure 11: Austenization in "fast" heating conditions: BCC phase fraction in 17-4PH steel (as-built SLM and re-austenitized SLM) obtained using neutron diffraction as a function of temperature during heating to 1050°C at 50K/min and maintaining for 30 minutes. The acquisition time was 30 s per pattern. The two materials have the same composition but different initial microstructure (ferrite and martensite).

Figure 12 shows the (110) BCC diffraction line for the three materials studied at room temperature and at 850°C. At room temperature, the wrought and re-austenitized SLM-ed materials have the broadest peaks. This is to be related to their martensitic microstructure. In a previous in-situ

diffraction study, it has been shown that martensitic transformation itself results in strong peak broadening [25]. It is then expected to have broad peaks on as-quenched martensitic microstructures. The as-built SLM-ed material shows a much finer peak, but it is still significantly broader than instrumental breadth. As this material has a ferritic microstructure, this broadening cannot be related to any martensitic transformation, but rather to plastic deformation related to the SLM process. Due to the very high cooling and heating rates experienced during SLM, high stresses can indeed develop in the part being built, resulting in plastic deformation. This has been confirmed by thermomechanical simulation of SLM on a 15-5PH steel, showing cumulated plastic strains as high as 25% in the as-built state [50]. In addition, experimental studies on SLM-ed austenitic steels have shown very high dislocation densities in the range 10^{14} to 10^{15} m^{-2} [27–30] in the as-built state, which further confirms the occurrence of plastic deformation during SLM building.

At 850°C (Figure 12), strong peak refining is observed compared to 20°C for the three materials. At that temperature, the three materials show the same peak breadth, which is still slightly larger than instrumental breadth.

Figure 13(a) shows the (110) BCC peak breadth (FWHM) as a function of temperature during heating to 1340°C at 5K/min in the three 17-4PH steels studied. The initial peak breadth is the same (~ $1.5x10^{-2}$ Angstrom) for the two martensitic materials (wrought and re-austenitized SLM-ed), but is significantly lower (~ $6x10^{-3}$ Angstrom) for the ferritic as-built SLM-ed material. Peak refining is observed for all the materials above 550°C / 600°C. The three materials reach the same peak breadth (~ $4.5x10^{-3}$ Angstrom) at about 750°C. At 950°C / 1000°C, the peak breadth is still slightly higher than instrumental breadth (~ $3x10^{-3}$ Angstroms). In contrast, at very high temperature (> 1200°C), the instrumental breadth is reached. The BCC peaks in the 1000°C - 1200°C range are absent or too small resulting in no data in Figure 13(a) in that temperature range.

Figure 13(b) shows the dislocation density determined from the peak breadth analysis for the three materials as a function of temperature. A comment is due first about the error on the dislocation

densities shown in this study. From Eq. (2), as the error on d is as low as about ~0.05%, the error on $\boldsymbol{\rho}$ arises mainly from the measurement of peak broadening β:

$$\frac{\Delta \boldsymbol{\rho}}{\boldsymbol{\rho}} \approx \mathbf{2}\frac{\Delta \boldsymbol{\beta}}{\boldsymbol{\beta_t - \beta_i}} \quad (5)$$

The random variations of the total peak breadth β_t observed in Figure 13(a) indicate that the $\Delta\beta/(\beta_t - \beta_i)$ term is of the order of 10%, except when the total peak breadth approaches the instrumental breadth, where the error is then significantly higher. The resulting error on ρ is of the order of 20% for $\rho \gtrsim 10^{14}$ m^{-2}. However, for $10^{13} \lesssim \rho \lesssim 10^{14}$ m^{-2}, when the total peak breadth is close to the instrumental breadth, the error on ρ can be of the order of a factor of 2 to 3.

The two martensitic materials (wrought and re-austenitized SLM) have an initial dislocation density of 5x10^{15} m^{-2}. This value is in very good agreement with previous measurements conducted on the same, or similar, materials using neutron or X-ray diffraction (4x10^{15} m^{-2} in [25] and [51]). It was shown in [25] that this dislocation density develops during the martensitic transformation itself because of the large change in volume between austenite and martensite. The initial dislocation density in the ferritic as-built SLM-ed material (4x10^{14} m^{-2}) is lower by a factor of ten compared to the two martensitic materials. It is however significantly above that in a well annealed material, which is of the order of 10^{11} to 10^{12} m^{-2} [52]. This shows that the SLM process produces significant plastic deformation during building. However the dislocation density produced by the SLM process itself is far below that resulting from the martensitic transformation. The value measured here for the ferritic as-built material (4x10^{14} m^{-2}) falls in the range obtained on as-built SLM-ed austenitic stainless steels (10^{14} - 10^{15} m^{-2} [26–29]). Figure 13(b) shows a decrease of the dislocation density upon heating from 550°C / 600°C, i.e. significantly before austenitizing starts. At about 750°C, the residual dislocation density is the same for the three materials (~ 2x10^{14} m^{-2}). Above 750°C, dislocation annihilation follows the same rate for the three materials, which results in identical data in Figure 13. It is to be noted that the dislocation density measured at 950°C / 1000°C, i.e. just before the BCC

peaks disappear, is about 10^{13} m^{-2}. This value is low but still measurable as it results in a BCC (110) peak breadth of $4x10^{-3}$ Angstrom, whereas the instrumental breadth is of $3x10^{-3}$ Angstrom.

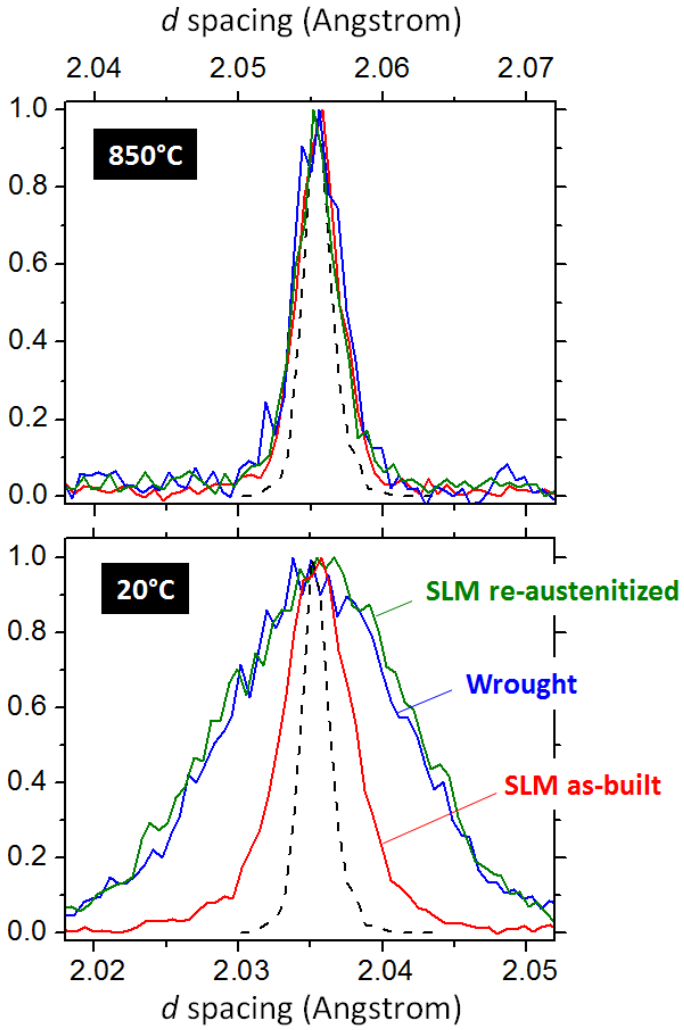

Figure 12: Normalized (110) diffraction line of the BCC phase obtained at room temperature and 850°C for the three 17-4PH steels studied (wrought, as-built SLM and re-austenitized SLM). The dotted line indicated the instrumental peak.

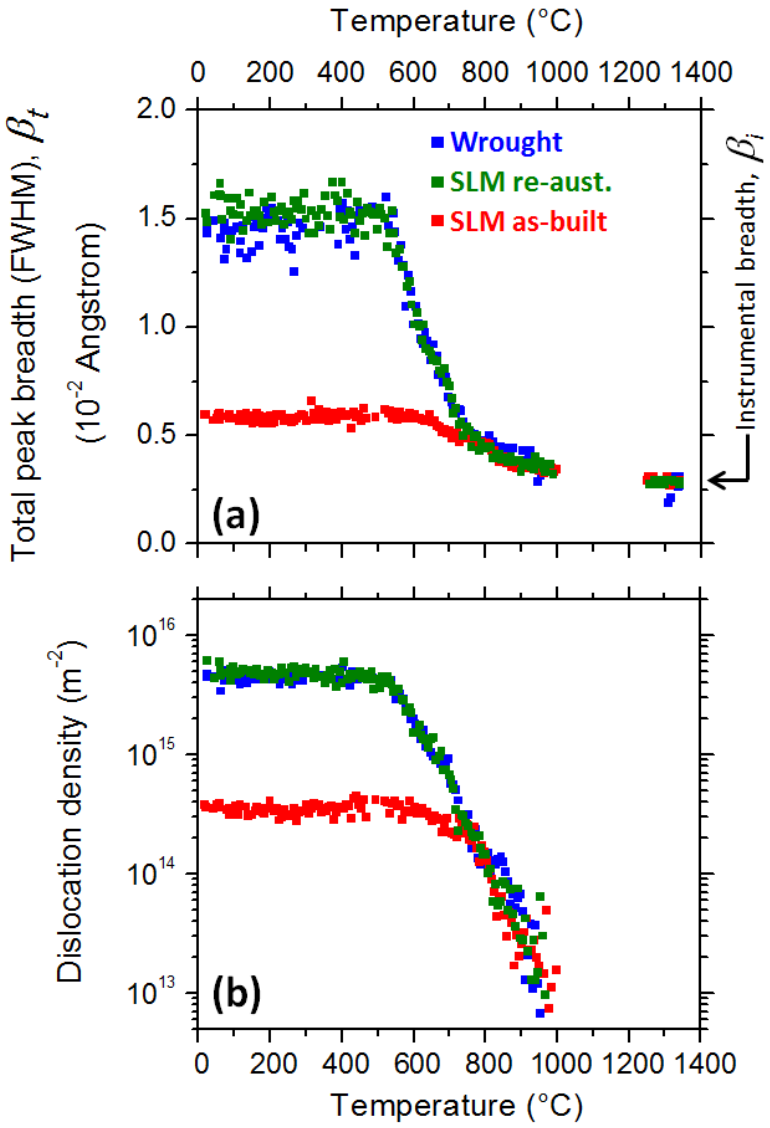

Figure 13: (a) Peak breadth of the BCC (110) line as a function of temperature for the three 17-4PH steels studied (wrought, as-built SLM and re-austenitized SLM) during heating to 1340°C at 5K/min. (b) Dislocation density estimated from Eq. 2.

Conclusions

In this paper, in-situ neutron diffraction measurements were used to monitor bulk phase transformations and dislocation density upon heating to very high temperature (i.e. close to the melting temperature) in 17-4PH steel with different compositions and/or different initial microstructures (wrought, as-built SLM-ed and re-austenitized SLM-ed). The main conclusions are summarized as follows:

- In contrast to the martensitic wrought steel, the microstructure of the as-built SLM-ed steel was found to be essentially ferritic. On the other hand, the re-austenitized SLM-ed steel recovered the martensitic microstructure.
- The existence of δ-ferrite at high temperature was experimentally demonstrated for the 17-4PH steel. This confirms the possibility for this steel to solidify mainly into δ-ferrite. However the amount of δ-ferrite at the melting temperature strongly depends on composition. In this study, the fractions of δ-ferrite at the melting temperature were 40% and 90% for the two steel compositions tested. The phase constitution obtained at the melting temperature are consistent with the nickel and chromium equivalents estimated from composition.
- Concerning the SLM process, solidification into austenite should be preferred to avoid the by-passing effect resulting in δ-ferritic microstructure, so as to obtain the desired martensitic microstructure in the as-built state. However this would require accurate adjustment of the amounts of BCC- and FCC-stabilizing elements. More research is needed to achieve this adjustment.
- The initial microstructure (ferrite or martensite) has little to no influence on re-austenization. At low heating rate, austenization takes places according to a two-step process.
- The ferritic as-built SLM-ed material contains a relatively high dislocation density (~$4x10^{14}$ m^{-2}), resulting from the SLM process. This is however far less than in the martensitic 17-4PH steel (~$5x10^{15}$ m^{-2}). Dislocations start to annihilate from 550°C / 600°C in all the materials studied, but a measurable dislocation density of ~10^{13} m^{-2} is still observed at 950°C / 1000°C.

Acknowledgments

Beam-time was awarded by the STFC ISIS facility under proposal number RB1810076 (doi:10.5286/ISIS.E.90682570). The staff of the Pressure and Furnace Section at the ISIS facility,

namely Chris Goodway, Paul McIntyre and Adam Sears, are kindly acknowledged for their work in preparing and setting-up the equipment for the neutron diffraction tests. The authors would like to acknowledge financial support from Institut CARNOT M.I.N.E.S (project #60678) and from LABEX MANUTECH-SISE (ANR-10-LABX-0075) of Université de Lyon, within the program "Investissements d'Avenir" (ANR-11-IDEX-0007) operated by the French National Research Agency (ANR). Max Boudes is kindly acknowledged for his help in EDX analyses.

Data availability statement

The raw and processed data required to reproduce these findings are available from the corresponding author upon request.

References

[1] W.D. Yoo, J.H. Lee, K.T. Youn, Y.M. Rhyim, Solid State Phenom. 118 (2006) 15–20.
[2] C.N. Hsiao, C.S. Chiou, J.R. Yang, Mater. Chem. Phys. 74 (2002) 134–142.
[3] U.K. Viswanathan, S. Banerjee, R. Krishnan, Mater. Sci. Eng. A 104 (1988) 181–189.
[4] L.E. Murr, E. Martinez, J. Hernandez, S. Collins, K.N. Amato, S.M. Gaytan, P.W. Shindo, J. Mater. Res. Technol. 1 (2012) 167–177.
[5] H.K. Rafi, D. Pal, N. Patil, T.L. Starr, B.E. Stucker, J. Mater. Eng. Perform. 23 (2014) 4421–4428.
[6] S. Cheruvathur, E.A. Lass, C.E. Campbell, JOM 68 (2016) 930–942.
[7] S. Vunnam, A. Saboo, C. Sudbrack, T.L. Starr, Addit. Manuf. 30 (2019) 100876.
[8] M. Alnajjar, F. Christien, K. Wolski, C. Bosch, Addit. Manuf. 25 (2019) 187–195.
[9] M. Alnajjar, F. Christien, V. Barnier, C. Bosch, K. Wolski, A.D. Fortes, M. Telling, Corros. Sci. 168 (2020) 108585.
[10] M. Alnajjar, F. Christien, C. Bosch, K. Wolski, Mater. Sci. Eng. A 785 (2020) 139363.
[11] E.A. Lass, F. Zhang, C.E. Campbell, Metall. Mater. Trans. A 51 (2020) 2318–2332.
[12] J.C. Lippold, D.J. Kotecki, Welding Metallurgy and Weldability of Stainless Steels, Wiley, 2005.
[13] F. Christien, M.T.F. Telling, K.S. Knight, Mater. Charact. 82 (2013) 50–57.
[14] R. Kapoor, I.S. Batra, Mater. Sci. Eng. A 371 (2004) 324–334.
[15] S.S. Babu, J.W. Elmer, J.M. Vitek, S.A. David, Acta Mater. 50 (2002) 4763–4781.
[16] P. Mayr, T.A. Palmer, J.W. Elmer, E.D. Specht, S.M. Allen, Metall. Mater. Trans. A 41 (2010) 2462–2465.
[17] H. Terasaki, Y. Komizo, Mater. Lett. 74 (2012) 187–190.
[18] M. Yonemura, T. Osuki, H. Terasaki, Y. Komizo, M. Sato, A. Kitano, Mater. Trans. 47 (2006) 310–316.
[19] J.W. Elmer, J. Wong, T. Ressler, Scr. Mater. 43 (2000) 751–757.

[20] Y. Tomota, Sci. Technol. Adv. Mater. 20 (2019) 1189–1206.
[21] C. Rowolt, B. Milkereit, M. Gebauer, C. Seidel, B. Müller, O. Kessler, HTM J. Heat Treat. Mater. 73 (2018) 317–334.
[22] J. Pešička, R. Kužel, A. Dronhofer, G. Eggeler, Acta Mater. 51 (2003) 4847–4862.
[23] R. Coppola, P. Lukáš, P. Mikula, M. Vrána, Phys. B Condens. Matter 241–243 (1997) 1261–1263.
[24] K. Macek, P. Lukáš, J. Janovec, P. Mikula, P. Strunz, M. Vrána, M. Zaffagnini, Mater. Sci. Eng. A 208 (1996) 131–138.
[25] F. Christien, M.T.F. Telling, K.S. Knight, Scr. Mater. 68 (2013) 506–509.
[26] J.S. Zuback, T. DebRoy, Materials 11 (2018) 2070.
[27] K. Akino, K. Kakehi, Mater. Trans. 59 (2018) 482–487.
[28] B.M. Morrow, T.J. Lienert, C.M. Knapp, J.O. Sutton, M.J. Brand, R.M. Pacheco, V. Livescu, J.S. Carpenter, G.T. Gray, Metall. Mater. Trans. A 49 (2018) 3637–3650.
[29] R. Pokharel, L. Balogh, D.W. Brown, B. Clausen, G.T. Gray, V. Livescu, S.C. Vogel, S. Takajo, Scr. Mater. 155 (2018) 16–20.
[30] S. Gorsse, C. Hutchinson, M. Gouné, R. Banerjee, Sci. Technol. Adv. Mater. 18 (2017) 584–610.
[31] F. Bachmann, R. Hielscher, H. Schaeben, Ultramicroscopy 111 (2011) 1720–1733.
[32] T. Nyyssönen, M. Isakov, P. Peura, V.-T. Kuokkala, Metall. Mater. Trans. A 47 (2016) 2587–2590.
[33] G. Kurdjumow, G. Sachs, Z. Für Phys. 64 (1930) 325–343.
[34] S. Morito, H. Yoshida, T. Maki, X. Huang, Mater. Sci. Eng. A 438–440 (2006) 237–240.
[35] F. Christien, D. Fortes, M. Alnajjar, M. Telling, STFC ISIS Neutron Muon Source (2018).
[36] O. Arnold, J.C. Bilheux, J.M. Borreguero, A. Buts, S.I. Campbell, L. Chapon, M. Doucet, N. Draper, R. Ferraz Leal, M.A. Gigg, V.E. Lynch, A. Markvardsen, D.J. Mikkelson, R.L. Mikkelson, R. Miller, K. Palmen, P. Parker, G. Passos, T.G. Perring, P.F. Peterson, S. Ren, M.A. Reuter, A.T. Savici, J.W. Taylor, R.J. Taylor, R. Tolchenov, W. Zhou, J. Zikovsky, Nucl. Instrum. Methods Phys. Res. Sect. Accel. Spectrometers Detect. Assoc. Equip. 764 (2014) 156–166.
[37] F. Akeroyd, S. Ansell, S. Antony, O. Arnold, A. Bekasovs, J. Bilheux, J. Borreguero, K. Brown, A. Buts, S. Campbell, D. Champion, L. Chapon, M. Clarke, S. Cottrell, R. Dalgliesh, D. Dillow, M. Doucet, N. Draper, R. Fowler, M.A. Gigg, G. Granroth, M. Hagen, W. Heller, A. Hillier, S. Howells, S. Jackson, D. Kachere, M. Koennecke, C. Le Bourlot, R. Leal, V. Lynch, P. Manuel, A. Markvardsen, R. McGreevy, D. Mikkelson, R. Mikkelson, R. Miller, S. Nagella, T. Nielsen, K. Palmen, P.G. Parker, M. Pascal, G. Passos, T. Perring, P.F. Peterson, F. Pratt, T. Proffen, P. Radaelli, J. Rainey, S. Ren, M. Reuter, L. Sastry, A. Savici, J. Taylor, R.J. Taylor, M. Thomas, R. Tolchenov, R. Whitley, M. Whitty, S. Williams, W. Zhou, J. Zikovsky, Mantid: Manipulation and Analysis Toolkit for Instrument Data., Mantid Project, 2013.
[38] A.C. Larson, R.B. Von Dreele, General Structure Analysis System, Los Alamos National Laboratory, 2004.
[39] B.H. Toby, J. Appl. Crystallogr. 34 (2001) 210–213.
[40] G.R. Stibitz, Phys. Rev. 49 (1936) 859–891.
[41] F.E. Haworth, Phys. Rev. 52 (1937) 613–620.
[42] W. Kurz, D.J. Fisher, Fundamentals of Solidification, Trans Tech Publications, Aedermannsdorf, Switzerland; Brookfield, Vt., 1992.
[43] S. Zhang, P. Wang, D. Li, Y. Li, Mater. Des. 84 (2015) 385–394.
[44] J. Yang, F. Huang, Z. Guo, Y. Rong, N. Chen, Mater. Sci. Eng. A 665 (2016) 76–85.
[45] S. Morito, X. Huang, T. Furuhara, T. Maki, N. Hansen, Acta Mater. 54 (2006) 5323–5331.
[46] Y. Sun, R.J. Hebert, M. Aindow, Mater. Des. 156 (2018) 429–440.
[47] A. Bojack, L. Zhao, P.F. Morris, J. Sietsma, Metall. Mater. Trans. A 47 (2016) 1996–2009.
[48] G.V. Raynor, V.G. Rivlin, Phase Equilibria in Iron Ternary Alloys: A Critical Assessment of the Experimental Literature, The Institute of Metals, London, 1988.
[49] H. Okamoto, ASM international, Alloy phase diagram committee, Asm international, Handbook committee, ASM Handbook. Volume 3, Volume 3, Binary Phase Diagrams, ASM International, Materials Park, Ohio, 2016.
[50] L. Van Belle, G. Vansteenkiste, J.C. Boyer, Key Eng. Mater. 504–506 (2012) 1067–1072.

[51] F. Niessen, D. Apel, F. Danoix, J. Hald, M.A.J. Somers, Mater. Charact. 167 (2020) 110494.
[52] G.K. Williamson, R.E. Smallman, Philos. Mag. 1 (1956) 34–46.